High Harmonic Generation Lab

Anton Johansson
Harald Öhrn

Supervisor: Felipe Zapata Abellan

February 2021

1 Introduction

In this laboratory exercise high order harmonic generation (HHG) is studied in the context of producing attosecond time-scale laser pulses for the study of ultra fast processes. Light propagating through a medium will cause the electrons to oscillate, in turn emitting radiation in the same frequency as the driving field. On the other hand, assuming a weak electromagnetic field, a perturbative treatment of the phenomena shows that multiples of the base frequency are also emitted (harmonics). This result is however not applicable to short pulses that reach the same amplitudes as the atomic potential, thus invalidating the assumption that the perturbation is small.

Therefore, the generation of high harmonics by short laser pulses needs to be examined by a semi-classical theoretical approach. This model will then be used to perform simulations of HHG spectra, as well as the resulting attosecond laser pulse. Finally, the simulations will be compared to experimental results obtained with the RABBIT-technique.

2 Theoretical Background

2.1 Semi-classical three-step model of HHG

For high amplitude laser fields one must consider higher order process in the light-mater interaction. To do this, the semi-classical three step model will be used. This model considers the quantum mechanical system of the valence electron trapped by the atom's coulomb potential, but treats the electron as a classical particle once it moves with the EM-field away from the atom. We will see that it is a good approximation, as the electrons path through the medium is long in comparison with the interaction range with the atom.

Consider an electron bound to an atom in a laser field linearly polarized in the x-direction, described by $V = E_0 sin(\omega t)x$. The shape of such an potential is shown in Fig. 1 (in one dimension). If the laser field is strong enough there will be a non negligible probability for the bound state to undergo tunnel ionization. This is the first steep in the three step model.

Once the electron is ionized it will be treated with classical mechanics. In addition, the width of the tunnel ionization is neglected and the ionization is assumed to occur

at the origin. In this simplified model for linearly polarized light, movement in all other directions is likewise neglected. The trajectory of the electron is given by Newtons second law,

$$m_e \ddot{x} = -e E_0 sin(\omega t), \tag{1}$$

where ω is the frequency of the laser field. To a good approximation this is an initial value problem with: $x(t_i) = 0, \dot{x}(t_i) = 0$, where t_i is time of ionization. Solving for $x(t)$ gives:

$$v(t) = \dot{(x)}(t) = -\frac{E_0}{\omega_0} sin(\omega_0 t) + C \tag{2}$$

$$V(t_i) = 0 \; \forall \; t_i \Rightarrow C = \frac{E_0}{\omega_0} sin(\omega_0 t_i) \tag{3}$$

$$x(t) = \frac{E_0}{\omega_0^2} \left(cos(\omega_0 t) + t\omega_0 sin(\omega_0 t_i)0 + \tilde{C} \right) \tag{4}$$

$$x(t_i) = 0 \; \forall \; \Rightarrow x = \frac{E_0}{\omega_0^2} \left(cos(\omega_0 t) + \omega_0(t - t_i)sin(\omega_0 t_i) - cos(\omega_0 t_i) \right) \tag{5}$$

Figure 2 shows Eq. 5 for different initial times. One notices that some trajectories bring the electron back to the atom at a later time. Indeed, most of these appear to cross the origin several times and will have a different velocity as they pass over the ion depending on the path taken. The accumulated kinetic energy as a function of ionization and recombination time is visualized in Fig. 2. Electrons that gain too much kinetic energy never recombine with the atom and the maximum kinetic energy is found to be $3.17U_p$, where $U_p = \frac{e^2 E_0^2}{4m_e\omega_0^2}$ is called the ponderomotive energy. From Fig. 2 one sees that we will have two trajectories for each kinetic energy, a short trajectory that starts late and recombines early and one long that starts before the short and ends after it. There also exists higher order recombination terms for trajectories traveling longer than one full laser field period. Figure 4 shows trajectories for different ionization times and the accumulated kinetic energy of each trajectory, clearly showing the difference between the long and short trajectories.

The last step of the three step model is recombination of the free electron back into an atomic bound state. This is once again a quantum mechanical view on the system. Once again it is assumed that the electron only interact with the atom as it passes the origin. Note also that the atom is assumed to be stationary between ionization and recombination. When the electron is absorbed it will emit a photon with energy $I_p + E_{kin}$, where I_p is the ionization potential of the atom's first valence electron.

Importantly, the maximum harmonic order q_{max} may now be estimated in the following way. Using a laser of peak intensity I corresponding to an electrical field of strength $E_0 = \sqrt{2I/(\epsilon_0 c)}$, the ponderomotive energy U_p can be calculated. For a given ionization energy I_p, the maximum order then becomes $q_{max} = (I_p + 3.17U_p)/(\hbar\omega_0)$, where ω_0 is the angular frequency of the laser.
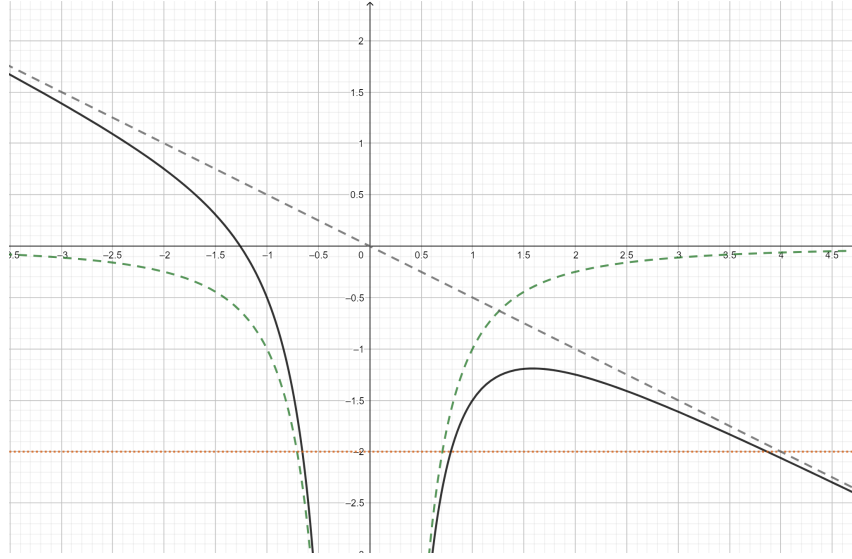
Figure 1: **A schematic view of the atomic potential in a strong laser field.** The laser field is expanded to first order as a potential linear in x with a oscillating slope. The bound state energy (doted line) is such that tunneling through the modified potential during some phase of the laser field would be possible.
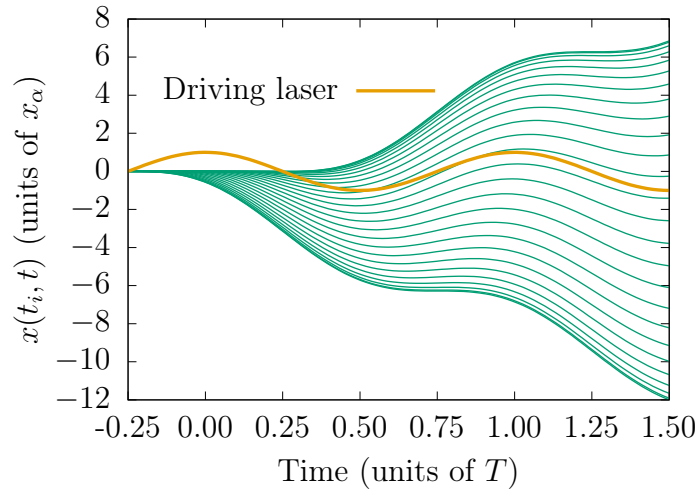

Figure 2: Electron trajectories $x(t_i, t)$ with $t_i \in [-0.25, 0.25]$ and for $t \in [-0.25, 1.5]$ along with the driving laser field in yellow. T is the period of the driving field. Note that some paths cross the zero-line several times while others never cross it.
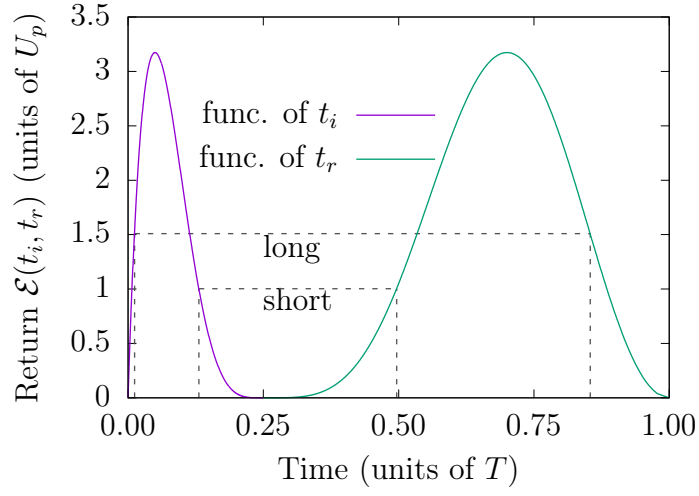
Figure 3: Kinetic energy $\mathcal{E}(t_i, t_r)$ as a function of both t_i and t_r along with the long trajectory for $\mathcal{E} = 1.5 U_p$ and short for $\mathcal{E} = U_p$. The maximum accumulated energy for any path that can recombine with the atom is $3.17\ U_p$.
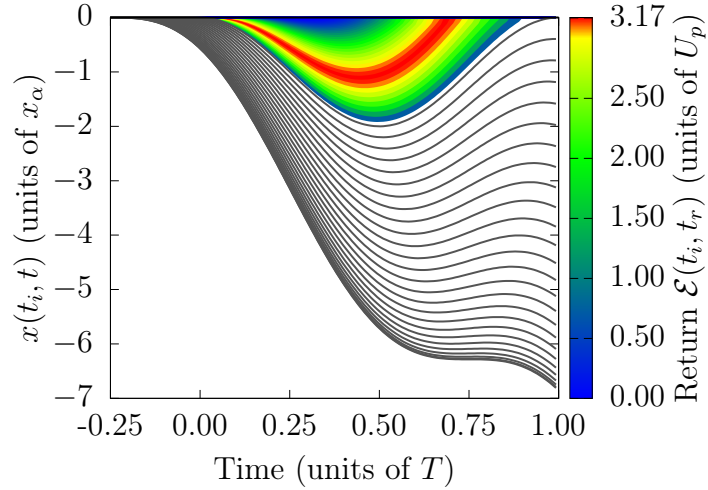

Figure 4: Same as Figure 2 however for more ionization times t_i. Trajectories that return to $x = 0$ has been colored with their kinetic energy upon return.

2.2 Attosecond pulse train model

We chose to describe the attosecond pulse train using the frequency of the involved harmonics. This approach treats the harmonics as monochromatic fields with a total pulse intensity given by:

$$I^{(\mathrm{HHG})}(t) \approx \left| \sum_{q \text{ odd}} A_q \exp[i(q\omega_0 t + \varphi_q)] \right|^2. \tag{6}$$

Here q is the harmonic order, A_q is the amplitude of of harmonic q and φ_q is the harmonic phase. Let $\Delta\varphi_{q+1} = \varphi_{q+1} - \varphi_q$ be the phase difference between two harmonics, this is the quantity of interest as the total harmonic phase is not experimentally determinable.

Figure 5 show how the total intensity vary with time for different q dependencies of the phase, for $A_q = 1$ and $q = 13$ to 21. The last of these figures have a positive q-dependence for $\Delta\varphi_{q+1}$ and is said to have a positive chirp. Similarly, a strictly negative q-dependence would result in negative chirp.
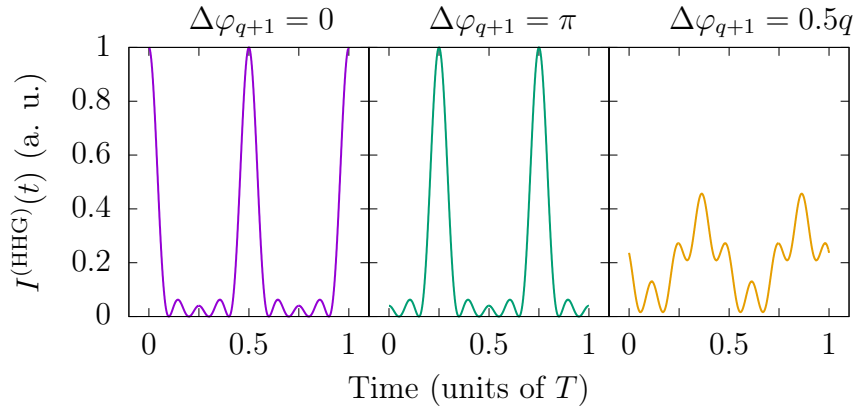

Figure 5: Intensity $I^{(\mathrm{HHG})}(t)$ for times $t \in [0, 1]$ and three types of φ_q dependence, expressed as $\Delta\varphi_{q+1} = \varphi_{q+2} - \varphi_q$.

3 Methodology

3.1 Simulations

For the numerical portion of this lab an ab initio approach developed by Ref. [1] was taken to solve the eigenvalue problem of the Hamiltonian $\hat{H}(t) = \hat{H}_0 + \hat{H}_{\mathrm{int}}(t)$ of a simple atom in a laser field. Where

$$\hat{H}_0 = -\frac{1}{2}\frac{\mathrm{d}^2}{\mathrm{d}x^2} - \frac{1}{\sqrt{x+a}}, \tag{7}$$

models the field-free atom, the regularization parameter a is used to avoid the pole at $x = 0$, and

$$\hat{H}_{\mathrm{int}} = -xE_0 \cos(\omega t), \tag{8}$$

describes the interaction with a light field in the dipole approximation. The light field was assumed to be polarized in the x direction. The stationary spectrum of the atom,

$\hat{H}_0|\psi_n\rangle = E_n|\psi_n\rangle$, was then solved by expanding the operator in a truncated B-spline basis and solving the associated matrix eigenvalue problem. This basis expansion requires numerical integration to compute the matrix elements which was done using a 20-point Gauss-Legendre scheme [2, 3]. Furthermore, descretizing the problem in time yields the time evolution of $|\psi\rangle$ as

$$|\psi(t + \Delta t)\rangle = \exp\left[-i\int_t^{t+\Delta t} \hat{H}(t')\mathrm{d}t'\right]|\psi(t)\rangle, \tag{9}$$

which was then solved using a Crank-Nicolson approach [2]. All time-propagation were done using the lowest energy state of $\hat{H}_0$ as an initial state.

After solving for $|\psi(t)\rangle$ for times $t \in [0, T]$, the HHG spectrum was obtained as the Fourier transform of the electron acceleration [2]. The HHG spectrum was studied for three laser intensities $0.5 \cdot 10^{14}$, $1.0 \cdot 10^{14}$, and $1.5 \cdot 10^{14}$ with the goal to compare simulations of the HHG cut-off order to predictions made by the semi-classical model.

Moreover simulations of the photoelectron spectra as induced by harmonics 15,17, and 19 was performed for three phase differences $\Delta\varphi_{q+1} = 0, 0.5, 0.5q$ with an IR field. The first case $\Delta\varphi_{q+1} = 0$ was also performed without any IR field.

3.2 Experimental setup and measurements

Regarding the experimental production and measurement of high harmonics, Fig. 6 presents as schematic representation of the setup used to achieve this. *Incoming beam* refers to a laser pulse created through Chirped Pulse Amplification (CPA) of a Ti:Sapphire laser with 1 kHz repetition rate. Typical output from the laser system is 2 mJ pulse with length 22 fs and wavelength 800 nm (IR).

The incoming beam first hits a Beam Splitter (BS) and is split into the *Probe beam* and *Active beam*, the latter is not indicated in the figure. Focusing firstly on the active beam which hits a *Focusing Mirror* (FM) with 50 cm focal length and is focused into a pulsed gas cell containing Argon at $3 \cdot 10^{-3}$ mbar pressure, indicated by (HHG), which is where the HHG takes place. The generated harmonics are then passed through an *Aluminium Filter* (AF) to block out remaining IR radiation. Following this was the *Recombination Mirror* (RM) with a small aperture for the harmonics to pass through, serving the dual purpose of recombining the harmonics with the probe beam and also filtering out harmonics emanating from long trajectories. This filtering of long trajectories was possible through their larger deviation from the center of the beam compared to shorter trajectories [2]. Next, the probe beam passed through a variable delay stage before recombining with the HHG the purpose of which is to determine the phase difference between the generated harmonics through the RABBIT technique.
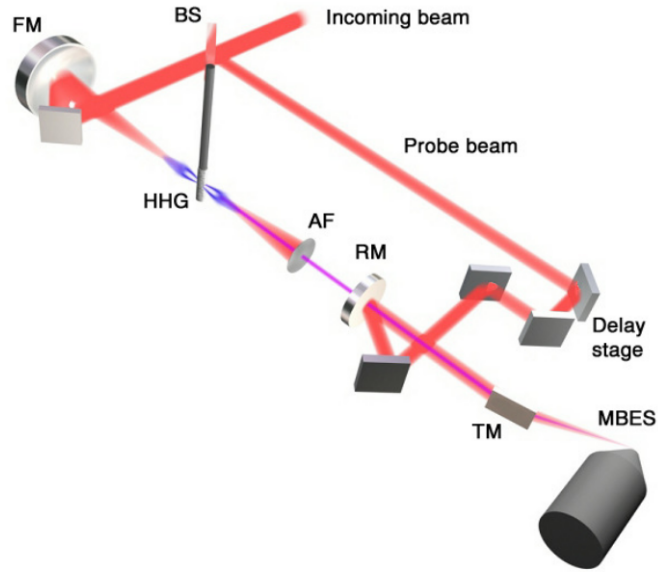
Figure 6: **Experimental setup for generation and measurement of high harmonics.**

The recombined high harmonic and probe beam then hit a *gold Toroidal Mirror* (TM) which refocuses the beam into the sensitive region of a *Magnetic Bottle Electron Spectrometer* (MBES). After which the beam interacted with the detection gas producing photoelectrons which after passing through a flight tube of length $\approx 200\,\mathrm{cm}$ was detected by a *Microchannel Plate*. Note that photoelectrons originating from harmonics with higher order q get larger kinetic energies and arrive first.

First, measurements of the photoelectron time-of-flight were performed for delays between the HHG pulse train and probe beam ranging from 20.0 ns to 29.8 ns. An incoming beam of wavelength $\lambda = 800$ nm ($\omega_0 = 0.057$ a.u. in atomic units) was used. Secondly, in order to calculate the kinetic energies of the photoelectrons, calibrations had to be made to account for the length of the flight-tube, which was estimated to be 2 m (precalibration). Lastly, from this the RABBIT-technique could be used to extract the relative phase differences between the harmonics and as such reconstruct the pulse train.

4 Results and discussion

4.1 Simulated bound and continuum electron states

First of all, the eigenvalue problem $\hat{H}_0|\psi_n\rangle = E_n|\psi_n\rangle$ for the time-independent Hamiltonian

$$\hat{H}_0 = -\frac{1}{2}\frac{\mathrm{d}^2}{\mathrm{d}x^2} - \frac{1}{\sqrt{x+a}}, \tag{10}$$

was solved using the approach outlined in Sec. 3.1 for $0 \leq x \leq 100$ a.u.. The wavefunction $|\psi_n\rangle$ is shown in Fig. 7 for $n = 0, 20$.
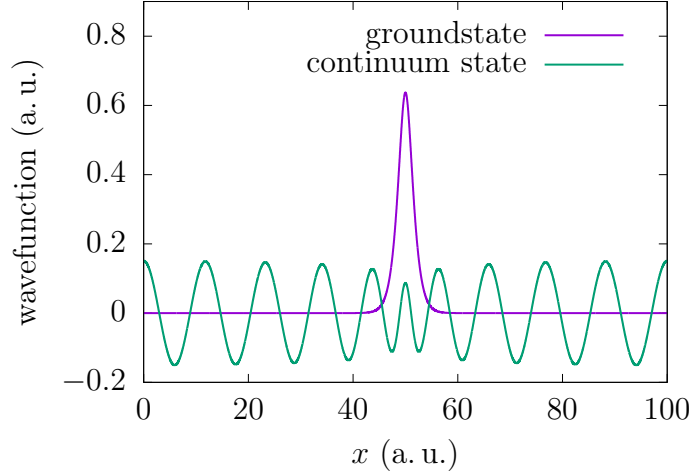
Figure 7: **Groundstate and contiuum state to Eq.** (10)**,** specifically states $|\psi_n\rangle$ for $n = 0$ and $n = 20$.

It becomes apparent that $n = 0$ corresponds to the bound electron groundstate whilst $n = 20$ corresponds to a contiuum state. Importantly, the figure shines a light on the importance of using a large spatial simulation region when dealing with contiuum states, since those states are not confined in space.

4.2 Simulation of high harmonic generation

Including the field interaction $\hat{H}_{\text{int}} = -xE_0 \cos(\omega t)$, the full Hamiltonian $\hat{H} = \hat{H}_0 + \hat{H}_{\text{int}}$ was solved using the method outlined in Sec. 3.1, for a simulation box of size $0 \leq x \leq 10^4$ and laser wavelength $\lambda = 800$ nm. Figure 8, 9 & 10 show the resulting HHG spectra for laser intensities $0.5 \cdot 10^{14}$, $1.0 \cdot 10^{14}$, and $1.5 \cdot 10^{14}$ W/cm^2 respectively.

In all three figures, a distinct peak is seen for lower order harmonics, as expected. This peak may be accounted for by a perturbative approach to problem which results in contributions for lower order harmonics. Figures 9 & 10 also show a clear plateau and cut-off region as expected. However, these region are hard to distinguish for the lower laser intensity in Fig. 8. Comparing the figures it also becomes clear that the cut-off increases with laser intensity, as predicted by the semi-classical three-step model.
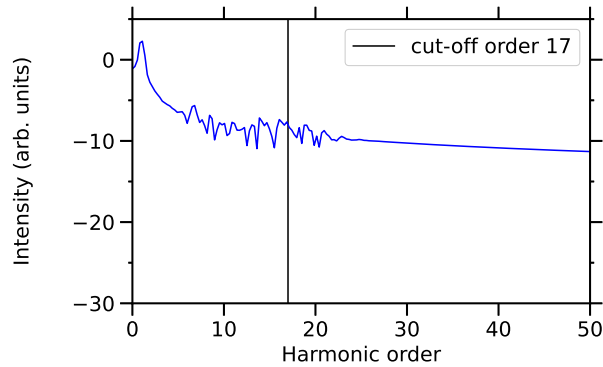

Figure 8: **Simulated HHG spectra using a laser intensity of** $I = 0.5 \cdot 10^{14}$ **W/cm**^{2}**.**

8

More specifically, the cut-off in Fig. 8 was estimated to be around order 17, whilst the three-step model predicts $q_{\max} \approx 16.3 \approx 17$ when rounded to closest odd integer, assuming an ionization potential of $I_p = 15.8$ eV.
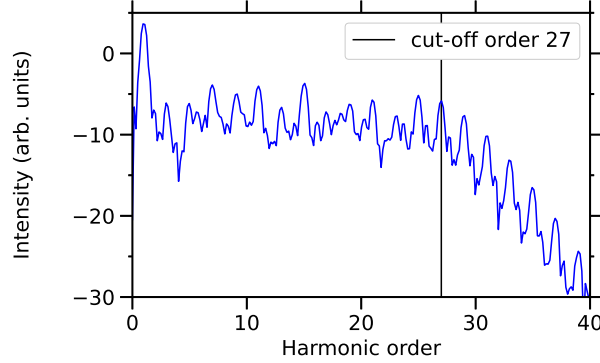

Figure 9: **Simulated HHG spectra using a laser intensity of** $I = 1.0 \cdot 10^{14}$ **W/cm^2.**

Similarly, for Fig. 9 the simulated cut-off order was estimated to 27, compared to 23 as predicted by the three-step model.
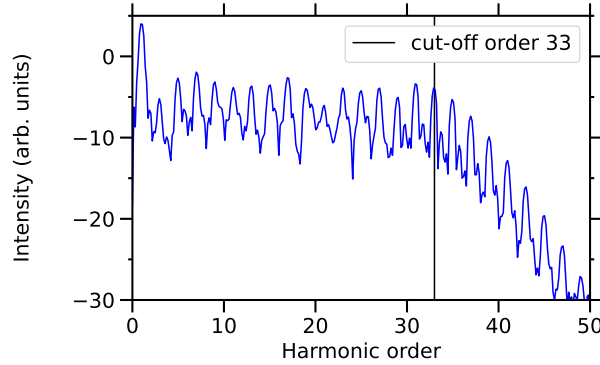

Figure 10: **Simulated HHG spectra using a laser intensity of** $I = 1.5 \cdot 10^{14}$ **W/cm^2.**

Lastly, the simulated cut-off order for Fig. 10 was 33 whilst the predicted value was 29. All in all the semi-classical three-step model is good in estimating the cut-off only being off by two orders!

4.3 Simulation of photoelectron spectra

Figure 11 presents simulated photoelectron spectra eminating from the interaction of harmonics 15,17, and 19 with the MBES detection gas. Simulations are done for a base IR wavelength of $\lambda = 800$ nm and three different phase dependencies $\Delta\varphi_{q+1} = 0, \Delta\varphi_{q+1} = 0.5$, and $\Delta\varphi_{q+1} = 0.5q$. For all three values of $\Delta\varphi_{q+1}$ the IR field was included in the simulation to study the appearance of side bands in the RABBIT method. Only $\Delta\varphi_{q+1} = 0$ is additionally included without an IR field, serving as a base case.
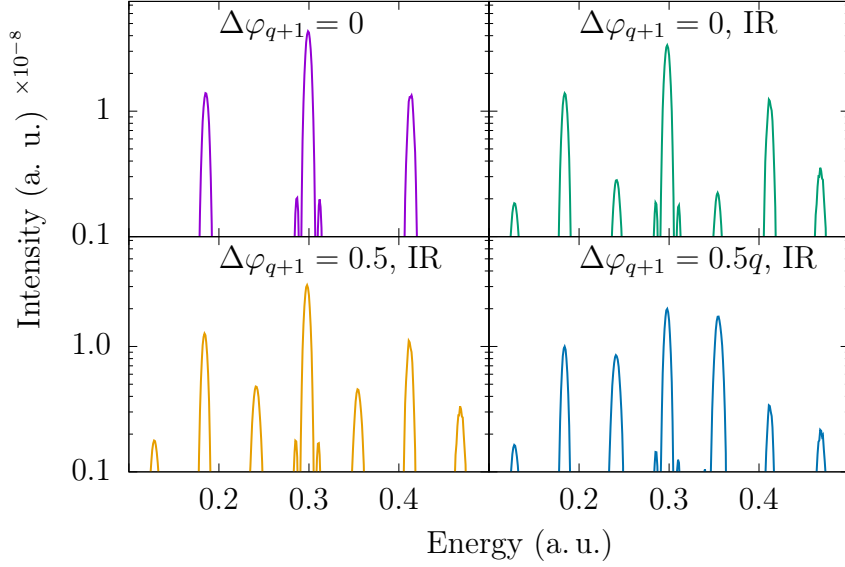
9

Figure 11: **Simulated photoelectron spectra of harmonics 15,17, and 19 with an underlying IR field.** Three phase dependencies of the pulse train $\Delta\varphi_{q+1} = 0, 0.5, 0.5q$ are included, and $\Delta\varphi_{q+1} = 0$ is also included without an IR field, serving as a base case.

Studying firstly the constant $\Delta\varphi_{q+1} = 0$ phase dependence without an IR field, three main bands at roughy $E = 0.2, 0.3, 0.4$ are clearly visible corresponding harmonics 15, 17, and 19 respectively, as expected. Moreover changing to a linear phase dependence ($\Delta\varphi_{q+1} = 0.5$) does not alter the shape of the main bands, which is expected as a linear phase dependence does not alter the shape nor frequency of the incoming pulse train, but only translates it in time (see Fig. 5). This in contrast to the main bands in the quadratic ($\Delta\varphi_{q+1} = 0.5q$) case where the intensity has shifted corresponding to a different more complicated pulse train shape, also present in Fig. 5.

Next, four side bands appear in between the three main bands when the IR field is switched on, in accordance with theory since the predicted energy gap between main bands is $2\hbar\omega_0$ where ω_0 is the IR frequency. Furthermore, comparing side band intensities between the constant and linear phase dependence cases shows that the two central side bands appear to increase in intensity by a similar amount whilst the edge side bands remain constant in intensity. This is expected, as the central side bands can be reached energetically through two paths: first absorbing a 15:th/17:th harmonic photon and then absorbing/emitting an IR photon. Meaning the intensity of the side band depends on the relative phase of the main bands next to it. This is in contrast to the edge side bands which may only be reached energetically through a single path and thus only depends on the absolute phase of the closest main band.

4.4 Phase extraction and pulse reconstruction

The RABBIT scan gives data as signal intensity for a range of photoelectron TOF and harmonic-to-probe time delay. To convert to energy the data was first calibrated. The

exact flight tube length is not known so a length correction factor γ is introduced, giving a total effective flight length of $L + \gamma$, where L is assumed to be 2 m. To calibrate, the well known frequency of the driving laser field ($\omega_0 = 0.057$ au) is used. The center-TOF for each band and sideband in the RABBIT scan is determined by integrating over signal delay, Fig. 12. The kinetic energy of a given TOF and γ is calculated as,

$$E_{kin} = m_e \frac{(L + \gamma)^2}{2t_{TOF}}. \tag{11}$$

A calibration score based on the average difference kinetic energy between neighbouring bands compared to ω_0 was computed and then minimized numerically to determined the true value of the calibration factor to be,

$$\gamma_{cal} = -0.3568 \text{ m}. \tag{12}$$

The signal for each sideband, as a function of probe-delay, is fitted to a general cos-function to extract its phase. The linear trend of the phase with higher order sidebands was computed, see Fig. 13. From this, the phase difference of a single harmonic could be calculated:

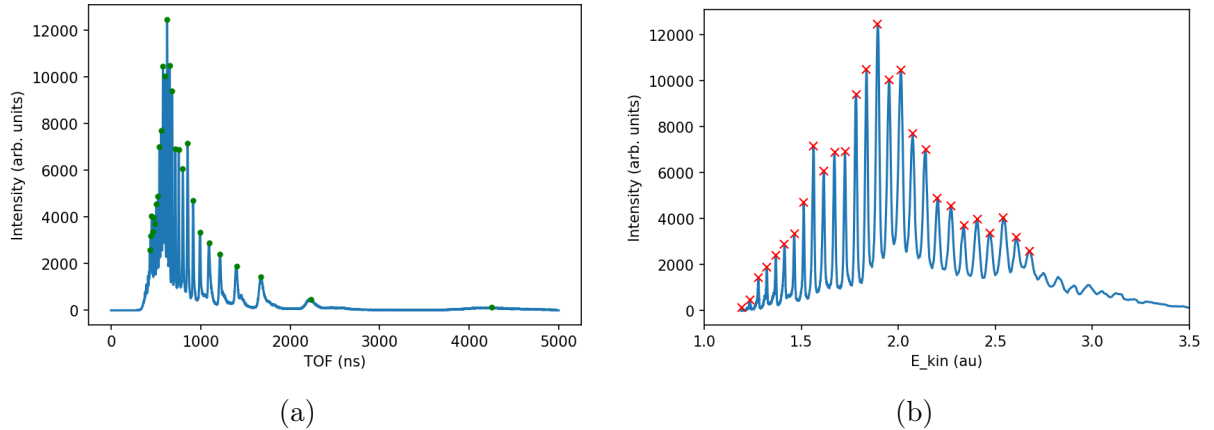$$\Delta\phi_{q+1} = 0.1157(108) \text{ rad}. \tag{13}$$

(a) (b)

Figure 12: **Raw RABBIT data integrated over harmonic delay (a) and the corresponding calibrated spectra (b).** The integrated spectra was used to determine the TOF for each band peak. Note that the low energy peaks in the calibrated spectra are the peaks with high TOF.

The harmonics detected in the RABBIT scan was determined to be $q = [21, 49]$ by analysing their respective kinetic energy and their relative intensity. The relative amplitude of each harmonic are the last values needed to reconstruct the attosecond pulse, these can be extracted from the scan data without much trouble. The attosecond pulse is reconstructed exactly as in Sec. 2.2 and is presented in Fig. 14.
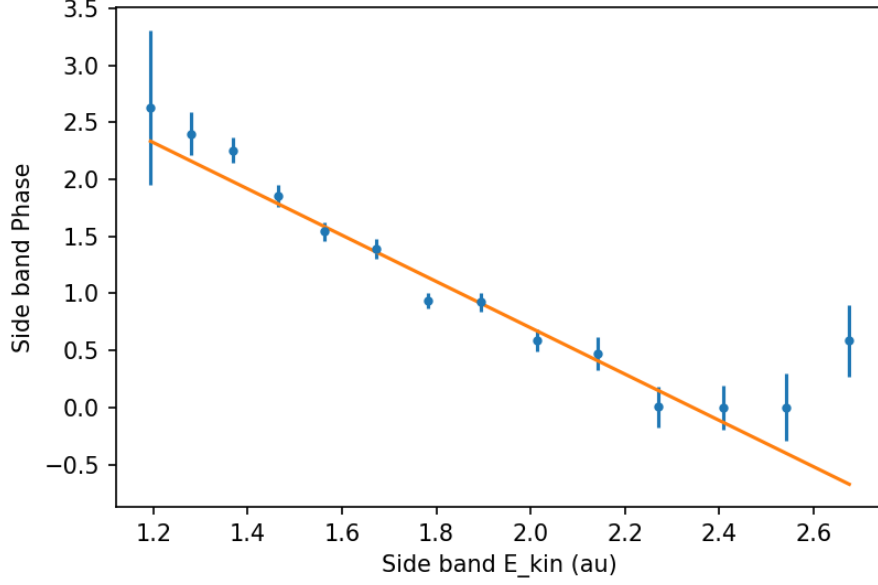
Figure 13: **Energy dependence of the RABBIT side band signal phase.** The weaker signal of the first and last couple of visible sidebands resulted in a substantial increases in relative errors associated with them. A clear linear dependence of the phase on the energy (or harmonic number) is seen in the high signal strength region of the graph. The solid line shows a least squares linear fit from which $\Delta\phi_{q+1} = 0.1157(11)$ rad can be extracted.
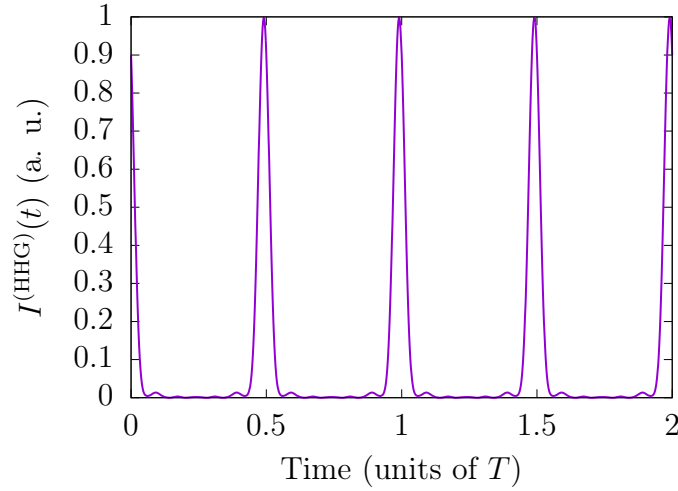

Figure 14: **Attosecond pulse reconstruction.** Using Eq. (6) for odd harmonics q in the range $21 \leq q \leq 45$ with the phase difference $\Delta\varphi_{q+1} = 0.1157$ rad and amplitudes measured amplitudes A_q. An initial phase of $\varphi_{21} = 0$ was assumed. Data normalized to a peak-intensity of 1 a. u..

5   Conclusion

We have used an ab initio numerical approach to simulate HHG and photoelectron spectra present in RABBIT measurements. This was followed by an experiment, creating a

photoelectron spectra with high order harmonics generate with Argon. This spectra was then analyzed with the RABBIT technique to reconstruct the laser pulse created from HHG.

Our simulated HHG spectra presented in Fig. 8, 9 & 10 for three laser intensities, showed good agreement with what is theoretically predicted. All expected features of the spectra were correctly reproduced. Moreover the exhibited cut-off orders were agreement with calculations in the semi-classical three-step model. Similarly, our simulated photoelectron in Fig. 11 shows the correct apparition of main and side bands, and their intensities varied with the phase dependence of the HHG pulse train in a manner predicted by theory.

The largest challenge of the RABBIT technique proved to be determining the side band phase as it involved fitting a function to a quite limited data set. This was especially evident for harmonics with a weak overall signal and if one compares Figs. 12 and 13, the correlation between weak signal and total error on the phase is fairly obvious. For these reasons we believe that the best way to enhance the accuracy of the RABBIT scan results would be to improve the fidelity of the pulse delay change. Our measurement used a 0.2 fs pulse-probe delay change between each "row" of the scan, compared to a 2.7 fs period of our probe light. We see a strong linear correlation for the phase dependence in Fig. 13 which is an indicator of the pulse being very close to being transform limited[2]. Only for the highest energy sidebands does $\Delta\phi_{q+1}$ appear to vary with q, even there it is difficult to say with a lot of certainty as the errors in that region are quite large. We would tentatively say that the true shape of the attosecond pulse would have a slight positive chirp in contrast to the reconstruction in Fig. 14.

References

[1] F. Zapata, *Electron dynamics induced by single and multiphoton processes in atoms and molecules*. PhD thesis, Sorbonne Université, 2019.

[2] F. Zapata, H. Laurell, D. Busto, and A. L'Huilier, *Atoms in Strong Laser Fields - Laboratory Manual*. P.O. Box 118, SE-22100 Lund, Sweden.

[3] A. Iserles, *A first course in the numerical analysis of differential equations*. No. 44, Cambridge university press, 2009.